

# I2I-Mamba: Multi-modal medical image synthesis via selective state space modeling

Omer F. Atli, Bilal Kabas, Fuat Arslan, Mahmut Yurt, Onat Dalmaz, and Tolga Çukur\*

**Abstract**—In recent years, deep learning models comprising transformer components have pushed the performance envelope in medical image synthesis tasks. Contrary to convolutional neural networks (CNNs) that use static, local filters, transformers use self-attention mechanisms to permit adaptive, non-local filtering to sensitively capture long-range context. However, this sensitivity comes at the expense of substantial model complexity, which can compromise learning efficacy particularly on relatively modest-sized imaging datasets. Here, we propose a novel adversarial model for multi-modal medical image synthesis, I2I-Mamba, that leverages selective state space modeling (SSM) to efficiently capture long-range context while maintaining local precision. To do this, I2I-Mamba injects channel-mixed Mamba (cmMamba) blocks in the bottleneck of a convolutional backbone. In cmMamba blocks, SSM layers are used to learn context across the spatial dimension and channel-mixing layers are used to learn context across the channel dimension of feature maps. Comprehensive demonstrations are reported for imputing missing images in multi-contrast MRI and MRI-CT protocols. Our results indicate that I2I-Mamba offers superior performance against state-of-the-art CNN- and transformer-based methods in synthesizing target-modality images.

**Index Terms**—medical image synthesis, modality, imputation, context, state space, sequence models, Mamba

## I. INTRODUCTION

Multi-modal medical images with distinct tissue contrasts provide complementary information about underlying anatomy, thereby boosting reliability in downstream analyses [1]. Multi-modal imaging is viable using different sequences on the same scanner or on entirely different scanners [2], albeit costs of running prolonged exams yield incomplete protocols under many clinical scenarios [3], [4]. As a remedy, target-modality images missing from a desired protocol can be synthesized based on the subset of source-modality images available [5], [6]. This synthesis task involves nonlinear transformation of signal levels between source and target images depending on tissue characteristics [7]–[9]. Although detailed tissue parameters that govern signal levels are generally unknown, a rudimentary prior on tissue composition

implicitly inferred from the spatial signal distribution in source images can guide such transformation [10]–[12]. Note that both healthy and pathological tissues can exhibit broad distribution in the form of spatially contiguous or segregated clusters across an anatomy [13], introducing not only local signal correlations in compact neighborhoods but also non-local signal correlations over extended distances [14]. Thus, successful solution of the synthesis task inherently rests on the ability to capture these short- and long-range contextual relations in medical images.

Over recent years, deep learning has emerged as the mainstream framework in medical image synthesis given its prowess in nonlinear function approximation [15]–[22]. In learning-based synthesis, a neural network model attempts to map source onto target images through hierarchical nonlinear transformations executed on intermediate feature maps [23], [24]. Naturally, the fidelity of the source-to-target mapping depends on the model’s expressiveness for the diverse set of contextual features encountered in medical images. Earlier studies in this domain have predominantly used CNN-based models that employ convolution operators for local, static filtering of feature maps [23]–[28]. The popularity of CNNs has been fueled by linear model complexity with respect to the dimensionality of the input image, and high expressiveness for local context that can be critical in synthesis of detailed tissue structure [29]–[39]. However, convolution operators that mediate these benefits also induce poor sensitivity to long-range contextual relations [40], [41]. In turn, CNNs can suffer from low synthesis accuracy near regions of heterogeneous tissue composition and uncommon pathology, where contextual relations often serve a key role in inferring the spatial distribution of tissue signals [42], [43].

Later studies have instead adopted transformer-based models based on self-attention operators that are capable of non-local, adaptive filtering [44]–[47]. Taking image patches as sequential tokens, transformers compute inter-token attention weights as similarity between token features and then use these weights to filter the input sequence non-locally. While self-attention operators increase sensitivity to long-range context, they induce quadratic model complexity with respect to sequence length (i.e., number of image patches), which can prohibit their use on small patches necessary to maintain high spatial precision [48]. Common strategies to permit the adoption of transformers in imaging tasks include approximations to attention operators to compress contextual representations that undesirably limit contextual sensitivity [46], [49], and tokenization via large patches (e.g., a  $16 \times 16$  image patch taken as a single token) that compromises spatial precision [47], [50]. Regardless, even these relatively more efficient

This study was supported by TUBA GEBIP 2015 and BAGEP 2017 fellowships awarded to T. Çukur (Corresponding author: Tolga Çukur, [cukur@ee.bilkent.edu.tr](mailto:cukur@ee.bilkent.edu.tr)).

O.F. Atli, B. Kabas, F. Arslan and T. Çukur are with the Department of Electrical and Electronics Engineering, Bilkent University, Ankara, Turkey (e-mails: {faruk.atli, bilal.kabas, fuat.arslan}@bilkent.edu.tr). T. Çukur is also with the National Magnetic Resonance Research Center (UMRAM), and the Department of Neuroscience, Bilkent University, TR-06800 Ankara, Turkey.

O. Dalmaz and M. Yurt are with the Department of Electrical Engineering, Stanford University, CA 94305, United States (e-mails: {onat.myurt}@stanford.edu).

variants of transformer models are often more complex than their CNN counterparts, which causes suboptimal learning on modest-sized training datasets common to medical imaging. An emerging alternative to capture long-range context under linear complexity with respect to sequence length is state-space sequence models (SSM) [51]–[54]. Few recent imaging studies have reported promising results based on a selective SSM variant (Mamba) in downstream tasks such as medical image segmentation [55]–[57] and classification [58]. Yet, the potential of SSMs for imputation of missing modalities in multi-modal imaging protocols remains unexplored.

Here, we introduce a novel learning-based model for multi-modal medical image synthesis, I2I-Mamba, based on selective SSM. Starting off with a convolutional backbone, I2I-Mamba episodically fuses channel-mixed Mamba blocks and CNN blocks at select stages of its bottleneck. The proposed cmMamba blocks comprise SSM layers to learn context across the spatial dimension of feature maps, and channel-mixing layers to learn context across the channel dimension. This architectural design enables the proposed model to capture both short- and long-range context in medical images while maintaining model complexity on par with convolutional models. Comprehensive demonstrations are reported for imputing missing modalities in multi-contrast MRI and MRI-CT protocols. Our results indicate that I2I-Mamba offers superior performance against recent convolutional and transformer baselines. Code to implement I2I-Mamba is publicly available at <https://github.com/icon-lab/I2I-Mamba>.

### Contributions

- To our knowledge, we introduce the first SSM-based model that translates between multi-modal data to synthesize missing medical images.
- We introduce a network architecture that episodically injects novel channel-mixed Mamba blocks in its bottleneck to simultaneously learn context across spatial and channel dimensions of feature maps.
- We demonstrate that the proposed I2I-Mamba model offers performance benefits over convolutional and transformer methods in multi-modal image synthesis tasks.

## II. RELATED WORK

### A. Convolutional models

Learning-based methods for multi-modal medical image synthesis aim to capture contextual relationships among tissue signals in order to impute target from source images. Inevitably, success towards this aim depends on the abilities of the employed model architectures in extracting context from medical images. A mainstream architecture for medical image synthesis tasks has been CNNs that purely use convolution operators to extract short-range context, albeit CNNs are known to suffer from insensitivity to long-range context and poor generalization to atypical anatomy [40], [41]. Attempts at alleviating these limitations include the use of attention mechanisms in CNN backbones to modulate intermediate feature maps and increase focus on potentially problematic regions in terms of synthesis performance [37], [42], [43], [59]–[62].

However, recent work suggests that such multiplicative gating of feature maps with attention offers limited sensitivity for global context since the underlying feature maps are still derived via convolution operators initially [63]–[65].

### B. Transformer models

As a promising alternative, transformer-based architectures have been adopted in medical imaging to improve capture of long-range contextual relations among anatomical regions for both non-synthesis [50], [63], [64], [66] and synthesis tasks [44], [46], [47]. To avoid the prohibitive computational burden of pure transformer backbones, a group of methods have adopted relatively efficient transformer variants based on approximations to self-attention operators, such as locally windowed or low-rank attention operators [46], [49], [67]. While such approximations improve efficiency by lowering the dimensionality of contextual representations, this inevitably limit the sensitivity benefits of transformers in deriving long-range contextual features [46]. A second group of methods have instead adopted hybrid CNN-transformer architectures, where vanilla transformer modules were selectively used in model stages with low-spatial-resolution feature maps [47], [64], inevitably lowering spatial precision in contextual representations extracted from medical images. In summary, while previous transformer-based methods have helped push the envelope in contextual sensitivity and performance in medical image synthesis, they still remain susceptible to suboptimal learning efficacy due to large model sizes compared to CNNs.

### C. SSM models

Selective state-space models are an emerging paradigm in machine learning that promises to capture long-range context while avoiding the computational burden associated with transformers. Few recent studies in medical imaging have proposed SSM-based models for downstream tasks including segmentation [55]–[57] and classification [58]. These studies have commonly proposed UNet-style architectures that follow an hourglass-shaped encoder-decoder structure while missing a backbone stage entirely [68]. UNet-style architectures use progressive downsampling to dramatically lower the spatial resolution of feature maps at midpoint (e.g. 16x16 feature maps), yielding rather limited spatial precision in high-level latent representations derived from input images. In turn, this can evoke performance losses in medical image synthesis due to poor spatial precision [30]. In stark contrast to these recent SSM-based models, I2I-Mamba leverages a ResNet-style architecture where the encoder performs only modest downsampling to maintain high-level latent representations at relatively high spatial resolution (e.g. 64x64 feature maps) [69]. Furthermore, I2I-Mamba uniquely employs a deep, episodic bottleneck where cmMamba blocks are intermittently injected to distill task-relevant contextual information. Corroborating recent reports that compare UNet-style versus ResNet-style backbones for transformer architectures [47], we argue that the proposed architecture is better sculpted to perform the dense predictions required for multi-modal medical image synthesis tasks. Lastly, unlike other SSM-based models in

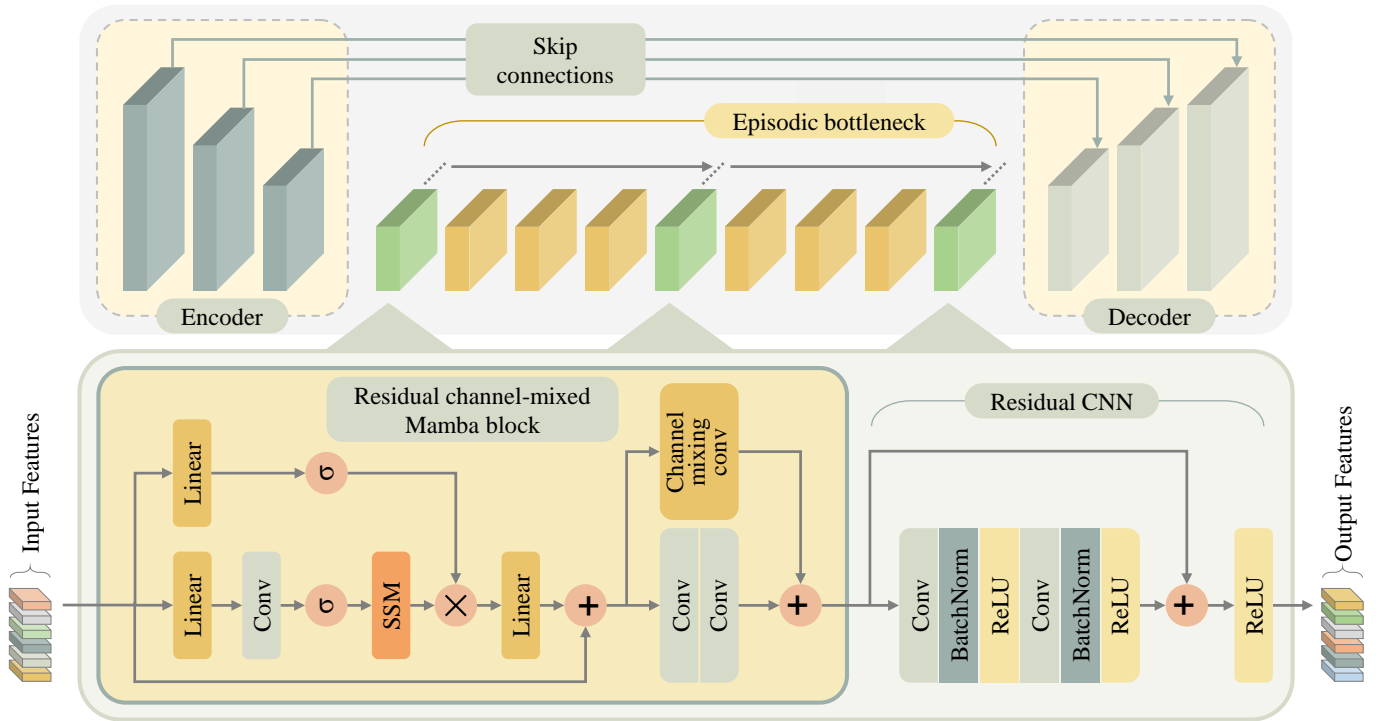


Fig. 1: Network architecture of I2I-Mamba. The proposed model comprises encoder, episodic bottleneck, and decoder modules to synthesize target-modality images from source-modality images. The encoder module extracts high-level latent representations of input images via convolutional layers. The episodic bottleneck extracts task-relevant contextual information from these representations: long-range spatial context and channel context via intermittent injection of residual channel-mixed Mamba blocks, and short-range spatial context via residual CNN blocks across all stages. The decoder module back-projects the contextualized representations onto the image domain via convolutional layers. Meanwhile, skip connections between respective encoder-decoder stages serve to relay low-level spatial representations.

medical imaging that analyze single-modality data, I2I-Mamba is devised to translate between separate imaging modalities.

### III. THEORY AND METHODS

#### A. I2I-Mamba

In this study, we introduce a novel learning-based model for multi-modal medical image synthesis. The proposed I2I-Mamba model leverages the sensitivity of SSMs to long-range context in conjunction with the local precision of CNNs to improve synthesis performance without introducing quadratic computational burden. Given the prowess of adversarial methods in medical image synthesis [30], here we implement I2I-Mamba as an adversarial model with generator and discriminator subnetworks. As depicted in Fig. 1, the generator comprises encoder, episodic bottleneck, and decoder modules to synthesize target-modality images given source-modality images as input. In the remainder of the section, we discuss the composition of each module and describe the learning procedures for I2I-Mamba.

**Model architecture:** Receiving as input source-modality images acquired within a multi-modal protocol, the encoder extracts high-level latent representations of input images. To construct the input to the encoder, available source images are concatenated across the channel dimension of an input tensor:

$$X = [x_1; x_2; \dots; x_I], \quad (1)$$

where  $I \in \mathbb{Z}^+$  denotes the number of source modalities,  $x_i \in \mathbb{R}^{H,W}$  denotes the source image for the  $i$ th modality, and  $X \in \mathbb{R}^{H,W,I}$  is the input tensor with  $H$ ,  $W$  denoting image height and width. The input tensor is projected through multiple CNN blocks to derive latent representations at moderate spatial resolution via modest downsampling:

$$L = \text{CNN}(X), \quad (2)$$

where  $L \in \mathbb{R}^{H'=H/\alpha, W'=W/\alpha, C}$  with  $\alpha$  denoting the degree of downsampling ( $\alpha = 4$  used here), and  $C$  denoting the number of feature channels. The encoder then relays these latent representations to the bottleneck module.

Receiving as input latent representations  $L$  from the encoder, the bottleneck extracts task-relevant contextual information from its input. For effective extraction, a deep bottleneck comprising a total of  $J$  stages is employed. As convolution operators are known for their high capability to capture short-range contextual features related to low-level image attributes, a residual CNN block is included at each stage [69]. Meanwhile, we utilize novel residual channel-mixed Mamba (cmMamba) blocks to capture long-range contextual features and benefit from input-adaptive filtering of latent representations. Here we observe that an episodic bottleneck design with intermittent injection of cmMamba blocks at the initial ( $j = 1$ ,  $j$  denoting stage index), middle ( $j = \lceil J/2 \rceil$ ), and final ( $j=J$ ) stages performs favorably. The  $j$ th bottleneck

stage receives input feature maps  $f_j \in \mathbb{R}^{H',W',C}$ , where  $f_j = L$  for  $j = 1$ . The mapping through this stage can be expressed as:

$$f_{j+1} = \begin{cases} \text{ResCNN}(\text{cmMamba}(f_j)) & \text{if } j = 1, \lceil J/2 \rceil, \text{ or } J \\ \text{ResCNN}(f_j) & \text{otherwise} \end{cases} \quad (3)$$

The cmMamba blocks contain SSM layers to capture long-range contextual information [52], and channel-mixing layers to capture relations between channels in feature maps [70]. In a cmMamba block,  $f_j$  is first tokenized into  $P = H'W'/p^2$  non-overlapping patches of size  $(p, p)$  to obtain a sequence  $z_{in}$ . In a first branch, the sequence is linearly embedded to compute a gating variable  $G$ :

$$G = \sigma(\text{Lin}(z_{in})), \quad (4)$$

where  $\sigma$  denotes an activation function. In a second branch, the sequence is linearly embedded, mixed via depth-wise convolution [71], and projected through an SSM layer:

$$M = \text{SSM}(\sigma(\text{DWConv}(\text{Lin}(z_{in}))))). \quad (5)$$

The SSM layer in Eq. 5 is implemented based on the selective state-space sequence model in [52]. Accordingly, the sequence of patches is first expanded via selective scans in multiple different directions across two-dimensional feature maps, the resultant sequence is processed via state-space modeling and then merged back. In this process, a discretized state-space model is construed:

$$h[n] = \mathbf{A}h[n-1] + \mathbf{B}z[n], \quad (6)$$

$$\bar{z}[n] = \mathbf{C}h[n] + \mathbf{D}z[n], \quad (7)$$

where  $h$  denotes the hidden state,  $z$  denotes the input sequence,  $\bar{z}$  denotes the output sequence,  $n$  is the sequence index,  $\mathbf{A} \in \mathbb{R}^{N,N}$ ,  $\mathbf{B} \in \mathbb{R}^{N,1}$ ,  $\mathbf{C} \in \mathbb{R}^{1,N}$ ,  $\mathbf{D} \in \mathbb{R}$  are learnable SSM parameters, and  $N$  is the dimensionality of state representations.

After gating  $M$  via a Hadamard product, it is linearly projected and residually combined with the input sequence:

$$z_{SSM} = z_{in} + \text{Lin}(G \odot M). \quad (8)$$

Note that  $z_{SSM}$  primarily reflects long-range spatial context between different image patches. To further capture context among separate feature channels,  $z_{SSM}$  is projected through a channel-mixing layer:

$$z_{cm} = \text{cmConv}(z_{SSM}) + \text{Conv}(z_{SSM}), \quad (9)$$

where channel mixing is achieved via a  $1 \times 1$  convolution operator [70]. The resultant sequence is then passed onto a residual CNN block to compute the output of the  $j$ th stage. Note that residual connections are used to externally propagate input feature maps around both SSM and CNN layers in the bottleneck stages. These connections serve to improve the preservation of a diverse array of features with varying levels of emphasis on short-range and long-range contextual features in medical images.

The decoder module receives as input contextualized feature maps  $f_j$  derived by the episodic bottleneck, and projects

them onto synthetic target image  $y \in \mathbb{R}^{H,W}$  via transposed convolutional layers:

$$y = \text{CNN}_{\text{transpose}}(f_j). \quad (10)$$

**Learning procedures:** Here, we devise I2I-Mamba as an adversarial model by including a conditional patch-based discriminator  $D$  [68]. The discriminator serves to distinguish actual target images ( $y_{act}$ ) from synthetic target images produced by the abovementioned generator ( $y_{syn}$ ). Assuming paired source-target images for subjects in the training set, a combined objective with pixel-wise and adversarial terms is used to train the generator  $G$ :

$$L_G = \lambda_{pix} \mathbb{E}[|y_{syn} - y_{act}|_1] - \lambda_{adv} \{ \mathbb{E}[D(y_{act}|X)^2] + \mathbb{E}[(D(y_{syn}|X) - 1)^2] \}, \quad (11)$$

where  $\mathbb{E}$  denotes expectation,  $y_{syn} = G(X)$ ,  $\lambda_{pix}$  and  $\lambda_{adv}$  are loss-term weightings. Meanwhile, an adversarial term is used to train the discriminator  $D$ :

$$L_D = \mathbb{E}[D(y_{act}|X)^2] + \mathbb{E}[(D(y_{syn}|X) - 1)^2]. \quad (12)$$

## B. Datasets

Experiments were conducted on a multi-contrast MRI dataset (IXI: <https://brain-development.org/ixi-dataset/>) and a multi-modal MRI-CT dataset [72].

1) *Multi-contrast MRI*: T<sub>1</sub>-, T<sub>2</sub>-, and PD-weighted brain MR images from 53 subjects were analyzed, with a (25, 10, 18) subject split for (training, validation, test) sets. In each subject, 100 cross-sections with brain tissue were included. Prior to modeling, T<sub>2</sub>- and PD-weighted images were spatially registered onto T<sub>1</sub>-weighted images via an affine transformation in FSL [73].

2) *MRI-CT*: T<sub>2</sub>-weighted MRI, and CT images of the pelvis from 15 subjects were analyzed, with a (9, 2, 4) subject split. In each subject, 90 cross-sections were included. As publicly shared, this dataset provides multi-modal images that are co-registered onto T<sub>2</sub>-weighted MRI scans.

## C. Competing Methods

We demonstrated I2I-Mamba against several state-of-the-art methods for medical image synthesis. Competing methods included convolutional models (pGAN, medSynth, SAGAN) and transformer models (ResViT, TransUNet, PTNet). For fair comparison, all competing methods were implemented as adversarial synthesis models by utilizing a PatchGAN discriminator and the loss functions in Eqs. 11-12.

1) *pGAN*: A convolutional model with a ResNet-based generator was considered [30].

2) *medSynth*: A convolutional model with a residual UNet generator was considered [32].

3) *SAGAN*: A convolutional model with self-attention modules incorporated into the generator was considered [43].

4) *ResViT*: A hybrid CNN-transformer model with ResNet-style backbone containing parameter-shared vanilla ViT modules was considered [47].



	$T_1, T_2 \rightarrow PD$		$T_1, PD \rightarrow T_2$		$T_2, PD \rightarrow T_1$		$T_2 \rightarrow PD$		$PD \rightarrow T_2$	
	PSNR	SSIM	PSNR	SSIM	PSNR	SSIM	PSNR	SSIM	PSNR	SSIM
I2I-Mamba	<b>35.55</b>	<b>0.972</b>	<b>35.71</b>	<b>0.970</b>	<b>30.39</b>	<b>0.951</b>	<b>34.81</b>	<b>0.969</b>	<b>34.99</b>	<b>0.970</b>
	$\pm 0.69$	$\pm 0.003$	$\pm 0.82$	$\pm 0.005$	$\pm 1.08$	$\pm 0.010$	$\pm 0.52$	$\pm 0.003$	$\pm 0.58$	$\pm 0.003$
pGAN	35.03	0.969	35.01	0.968	29.77	0.946	33.96	0.966	34.30	0.966
	$\pm 0.65$	$\pm 0.003$	$\pm 0.67$	$\pm 0.003$	$\pm 1.13$	$\pm 0.010$	$\pm 0.44$	$\pm 0.003$	$\pm 0.45$	$\pm 0.003$
medSynth	34.80	0.968	34.62	0.968	29.52	0.943	33.99	0.966	33.56	0.969
	$\pm 0.65$	$\pm 0.003$	$\pm 0.72$	$\pm 0.003$	$\pm 1.07$	$\pm 0.010$	$\pm 0.58$	$\pm 0.003$	$\pm 0.79$	$\pm 0.003$
SAGAN	34.27	0.965	34.56	0.966	29.30	0.944	34.03	0.965	34.01	0.965
	$\pm 0.63$	$\pm 0.003$	$\pm 0.68$	$\pm 0.003$	$\pm 1.17$	$\pm 0.010$	$\pm 0.41$	$\pm 0.003$	$\pm 0.42$	$\pm 0.003$
ResViT	35.01	0.970	34.49	0.966	30.19	0.950	34.49	0.969	34.87	0.969
	$\pm 0.49$	$\pm 0.002$	$\pm 0.50$	$\pm 0.003$	$\pm 1.15$	$\pm 0.010$	$\pm 0.44$	$\pm 0.003$	$\pm 0.49$	$\pm 0.003$
TransUNet	34.07	0.970	33.83	0.962	29.26	0.944	33.08	0.963	32.55	0.960
	$\pm 0.63$	$\pm 0.003$	$\pm 1.23$	$\pm 0.006$	$\pm 1.24$	$\pm 0.010$	$\pm 0.57$	$\pm 0.003$	$\pm 1.12$	$\pm 0.004$
PTNet	34.75	0.971	34.22	0.963	28.19	0.925	32.91	0.960	31.95	0.946
	$\pm 0.63$	$\pm 0.003$	$\pm 1.89$	$\pm 0.012$	$\pm 1.04$	$\pm 0.015$	$\pm 0.63$	$\pm 0.004$	$\pm 2.33$	$\pm 0.032$

TABLE I: Performance for many-to-one ( $T_1, T_2 \rightarrow PD$ ,  $T_1, PD \rightarrow T_2$ , and  $T_2, PD \rightarrow T_1$ ) and one-to-one ( $T_2 \rightarrow PD$  and  $PD \rightarrow T_2$ ) tasks in IXI. PSNR (dB) and SSIM are listed as mean $\pm$ std across the test set. Boldface indicates the top-performing model for each task.

5) *TransUNet*: A hybrid CNN-transformer model with UNet-style generator containing vanilla ViT modules was considered [64].

6) *PTNet*: A transformer model with a UNet-style generator containing efficient performer layers was considered [46].

#### D. Architectural Design

Receiving source-modality images as input, I2I-Mamba first projected its input through an encoder module with three stages. Each stage contained a CNN block with a convolutional layer, batch normalization, and ReLU activation. The encoded feature map of dimension  $\mathbb{R}^{256,64,64}$  was then projected through a bottleneck module with nine stages. Feature map dimensions were maintained constant across the episodic bottleneck. Each stage contained a residual CNN block comprising two cascades of a convolutional layer, batch normalization, and ReLU activation. Residual cmMamba blocks were episodically inserted in the initial, middle, and final bottleneck stages. Patches were embedded via a linear projection layer, followed by a convolutional layer, SiLU activation, and an SSM layer. The SSM output was multiplicatively gated and linearly projected, and then combined with the input feature maps relayed via a residual connection. Afterward, a channel-mixing block was inserted that used a parallel combination of a channel-mixing convolutional layer and two regular convolutional layers. Lastly, the context-embedded feature map of dimension  $\mathbb{R}^{256,64,64}$  was projected through a decoder module with three stages to synthesize target-modality images. Each stage contained a CNN block with a convolutional layer, batch normalization, and ReLU activation, except for the final stage that used a Tanh activation. Note that long-range skip connections were employed between corresponding stages of encoder and decoder modules, in order to better preserve low-level spatial information.

#### E. Modeling Procedures

Modeling was performed using the PyTorch framework on an Nvidia RTX 4090 GPU. Following random initialization of model weights, all models were trained via the Adam optimizer [74] with parameters  $\beta_1 = 0.5$ ,  $\beta_2 = 0.999$ . Model hyperparameters including learning rate ( $\eta$ ), number of epochs (E), and loss-term weights were selected via cross-validation. For each method, a single common set of hyperparameters was selected that yielded near-optimal validation performance across synthesis tasks. While  $\eta = 2 \times 10^{-4}$  was prescribed for all methods,  $E=60$  was selected for I2I-Mamba, ResViT, and  $E=100$  for remaining methods. To minimize potential biases due to variable loss functions, a common set of loss-term weights  $\lambda_{adv} = 1$ ,  $\lambda_{pix} = 100$  was prescribed for all methods. To quantitatively evaluate multi-modal synthesis performance, peak signal-to-noise ratio (PSNR) and structural similarity index (SSIM) metrics were measured. Measurements were taken between ground-truth and synthetic target-modality images. The significance of performance differences between competing methods was assessed with non-parametric Wilcoxon signed-rank tests ( $p < 0.05$ ).

## IV. RESULTS

### A. Multi-Contrast MRI Synthesis

We first conducted experiments for target-modality imputation in multi-contrast MRI. The proposed I2I-Mamba model was comparatively demonstrated against convolutional models (pGAN, medSynth, SAGAN), and transformer models (ResViT, TransUNet, PTNet). PSNR and SSIM metrics for many-to-one and one-to-one tasks are listed in Table I. I2I-Mamba achieves the highest performance metrics in all examined tasks ( $p < 0.05$ ). On average, I2I-Mamba outperforms convolutional models by 0.91dB PSNR and 0.41% SSIM, and

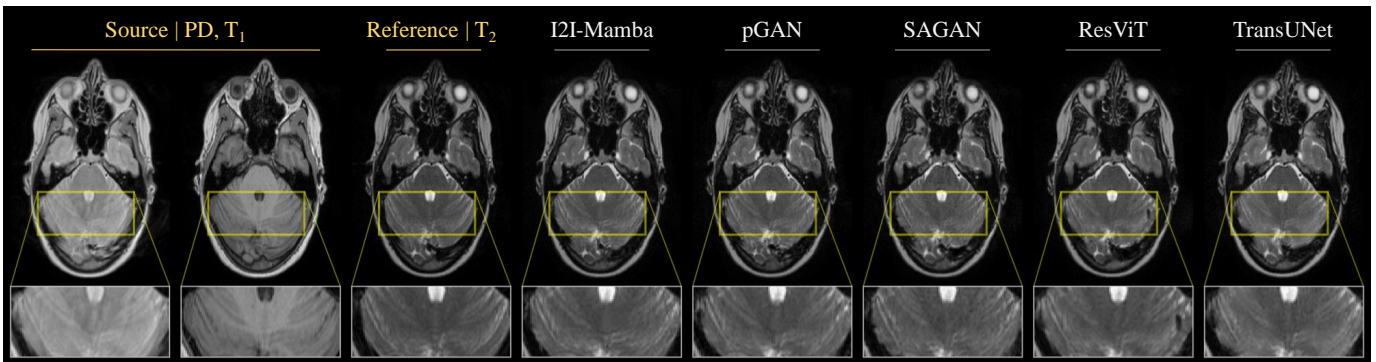


Fig. 2: Synthesis results for PD,  $T_1 \rightarrow T_2$ . Synthetic target images from competing methods are displayed along with source images and reference target images. Compared to baselines, I2I-Mamba generates images with lower artifact and noise levels and sharper depiction of tissue structure.

transformer models by 1.37dB PSNR and 0.72% SSIM. Representative synthetic target images for the PD,  $T_1 \rightarrow T_2$  task are displayed in Fig. 2 for I2I-Mamba and four top-contending baselines. Corroborating quantitative evaluations, we find that I2I-Mamba synthesizes target images with lower artifact levels and sharper tissue depiction than both convolutional and transformer baselines.

### B. MRI-CT Synthesis

Next, we conducted experiments for target-modality imputation in multi-modal MRI-CT. I2I-Mamba was again compared against convolutional models (pGAN, medSynth, SAGAN), and transformer models (ResViT, TransUNet, PTNet). PSNR and SSIM metrics for this synthesis task are listed in Table II. I2I-Mamba achieves the highest performance metrics among baselines ( $p < 0.05$ ). On average, I2I-Mamba outperforms convolutional models by 1.14dB PSNR and 1.50% SSIM, and transformer models by 0.75dB PSNR and 0.30% SSIM. Representative synthetic target images are displayed in Fig. 3 for I2I-Mamba and four top-contending baselines. Compared to baselines, I2I-Mamba synthesizes target images with lower artifacts and more accurate tissue structure, particularly for diagnostically relevant bone regions. Taken together, these results indicate that the elevated sensitivity of I2I-Mamba to long-range context combined with its low model complexity enables it to learn synthesis models for reliable imputation of missing medical image modalities.

## V. DISCUSSION

In this study, we proposed a novel image synthesis method to impute missing modalities in medical imaging protocols. Conventional CNN-based methods are insufficiently sensitive to relationships between distant anatomical regions in medical images [41]. While transformer-based methods employ self-attention operators to alleviate this limitation, they introduce quadratic computational complexity with respect to sequence length that typically restricts the use of transformer modules to low-resolution feature maps obtained by substantial down-sampling [64] or by tokenization via large image patches [47].

Unlike previous methods, I2I-Mamba combines the contextual sensitivity of SSMs with the local precision of CNNs to learn long-range relationships in medical images without elevating computational burden. Our results indicate that I2I-Mamba offers superior quantitative and qualitative performance in multi-modal medical image synthesis against previous CNN and transformer baselines.

Several lines of development can help further improve the proposed method’s performance. A first group of developments concerns the synthesis tasks implemented by I2I-Mamba. Here we examined one-to-one and many-to-one tasks to impute missing images in multi-contrast MRI and MRI-CT protocols. For optimal performance, a separate model was built for each individual task. In certain scenarios, missing and acquired modalities in a multi-modal protocol may vary sporadically across the imaging cohort [75]. To improve practicality in such cases, a unified I2I-Mamba can be generalized to flexibly implement many-to-many synthesis tasks by adopting a masking strategy and mixing training samples for different source-target configurations during modeling [47]. Recent work suggests that there may be potential benefits to fusing one-to-one and many-to-one mappings in terms of preserving modality-specific information during many-to-one synthesis tasks [38], [75]. Similarly, separate I2I-Mamba models trained for one-to-one and many-to-one tasks could be combined to improve sensitivity to the unique features in each modality. It may also be possible to boost generalization capabilities by decentralized training of multi-site synthesis models across multiple institutions with access to diverse datasets to enable reliable multi-tasking across distinct source-target configurations [76], [77]. Here, we performed supervised learning by assuming that a paired set of source-target images is available in each training subject [30]. In cases where training images for source versus target modalities are curated from different subjects, unsupervised learning strategies based on cycle-consistency could be adopted [78]–[80].

A second group of developments concerns the loss functions used for model training. For fair comparison among architectures, here we implemented all competing methods based on a combined pixel-wise and adversarial loss term [68].

		I2I-Mamba	pGAN	medSynth	SAGAN	ResViT	TransUNet	PTNet
MRI $\rightarrow$ CT	PSNR	<b>28.51</b>	27.22	26.87	28.03	27.87	28.06	27.35
		$\pm 1.94$	$\pm 2.73$	$\pm 1.79$	$\pm 1.97$	$\pm 2.06$	$\pm 2.20$	$\pm 2.23$
	SSIM	<b>0.916</b>	0.906	0.886	0.911	0.913	0.915	0.911
		$\pm 0.023$	$\pm 0.026$	$\pm 0.026$	$\pm 0.020$	$\pm 0.027$	$\pm 0.021$	$\pm 0.026$

TABLE II: Performance for the  $T_2$ -weighted MRI  $\rightarrow$  CT synthesis task in the MRI-CT dataset. Boldface indicates the top-performing model for each task.

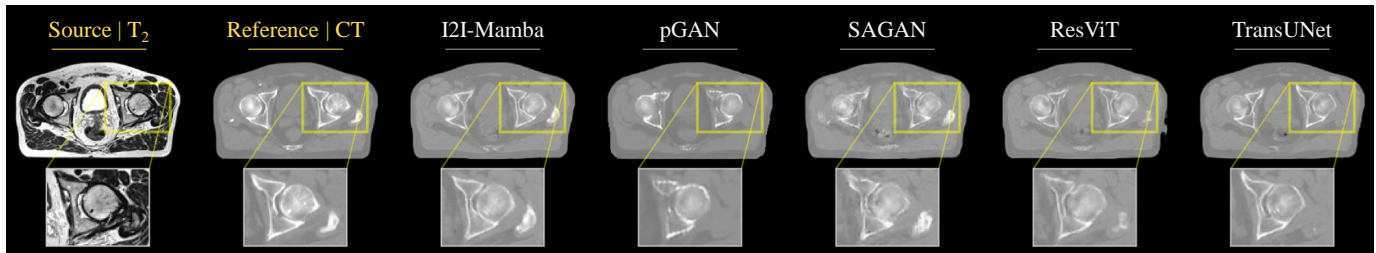


Fig. 3: Synthesis results for  $T_2$ -weighted MRI  $\rightarrow$  CT. Synthetic target images from competing methods are displayed along with source images and reference target images. Compared to baselines, I2I-Mamba generates a target image with lower artifact levels and more accurate tissue structure that is closely aligned with the reference image.

Corroborating recent reports in the literature [30], we observed that this combined loss provides models that can synthesize high-quality target images with detailed tissue structure. That said, it might be possible to attain further performance improvements by employing more advanced loss functions including gradient-based, difficulty-aware, cross-entropy losses [32], [81], [82]. A potential limitation of adversarial learning is instabilities in model training that can hamper the fidelity of synthetic images [83]. While we did not observe notable signs of instability in this work, diffusion-based learning techniques could be adopted to improve reliability when necessary [84]–[86]. The time-dependent mappings required in diffusion models could be attained via a time-embedding vector that could be used to modulate feature maps additively [84] or multiplicatively [87] at each network stage. Task-relevant information used during the training of diffusion models could be enhanced by employing diffusion bridge formulations relevant to medical image synthesis [88], [89]. Recent studies have shown stark advantages to combining diffusion-based learning with transformer architectures [90], [91]. It is likely that adopting I2I-Mamba in a diffusion framework would offer similar benefits without the computational overhead. Lastly, it might be possible to further improve the task-specific performance of I2I-Mamba by adopting pre-training of its SSM-based architecture [92]. Future studies are warranted for an in-depth evaluation of the ideal training procedures for I2I-Mamba.

## VI. CONCLUSION

Here we introduced a novel learning-based model for imputing missing modalities in multi-modal medical imaging protocols. I2I-Mamba leverages a hybrid architecture where

cmMamba and CNN blocks are residually fused across an episodic bottleneck, which maintains feature maps at moderate spatial-resolution for high spatial precision. The proposed cmMamba blocks comprise SSM layers to model spatial context and channel-mixing layers to model channel context. As such, the resultant architecture efficiently captures contextual relationships in medical images without the added computational burden of self-attention operators. With its superior performance over state-of-the-art convolutional and transformer baselines, I2I-Mamba holds great potential for multi-modal medical image synthesis.

## REFERENCES

- [1] B. J. Pichler, M. S. Judenhofer, and C. Pfannenberger, *Multimodal Imaging Approaches: PET/CT and PET/MRI*. Springer, 2008, pp. 109–132.
- [2] B. Moraal, S. Roosendaal, P. Pouwels, H. Vrenken, R. Schijndel, D. Meier, C. Guttman, J. Geurts, and F. Barkhof, “Multi-contrast, isotropic, single-slab 3d MR imaging in multiple sclerosis,” *Eur. Radiol.*, vol. 18, pp. 2311–2320, 2008.
- [3] B. Thukral, “Problems and preferences in pediatric imaging,” *Indian J. Radiol. Imaging*, vol. 25, pp. 359–364, 2015.
- [4] K. Krupa and M. Bekiesińska-Figatowska, “Artifacts in magnetic resonance imaging,” *Pol. J. Radiol.*, vol. 80, pp. 93–106, 2015.
- [5] J. E. Iglesias, E. Konukoglu, D. Zikic, B. Glocker, K. Van Leemput, and B. Fischl, “Is synthesizing MRI contrast useful for inter-modality analysis?” in *Med. Image Comput. Comput. Assist. Interv.*, 2013, pp. 631–638.
- [6] Y. Huo, Z. Xu, S. Bao, A. Assad, R. G. Abramson, and B. A. Landman, “Adversarial synthesis learning enables segmentation without target modality ground truth,” in *Int. Symp. Biomed. Imaging*, 2018, pp. 1217–1220.
- [7] D. H. Ye, D. Zikic, B. Glocker, A. Criminisi, and E. Konukoglu, “Modality propagation: Coherent synthesis of subject-specific scans with data-driven regularization,” in *Med. Image Comput. Comput. Assist. Interv.*, 2013, pp. 606–613.
- [8] C. Catana, A. van der Kouwe, T. Benner, C. J. Michel, M. Hamm, M. Fenchel, B. Fischl, B. Rosen, M. Schmand, and A. G. Sorensen, “Toward implementing an MRI-based PET attenuation-correction method for neurologic studies on the MR-PET brain prototype,” *J. Nucl. Med.*, vol. 51, no. 9, pp. 1431–1438, 2010.



- [9] S. Roy, A. Jog, A. Carass, and J. L. Prince, "Atlas based intensity transformation of brain MR images," in *Multimodal Brain Image Anal.*, 2013, pp. 51–62.
- [10] J. Lee, A. Carass, A. Jog, C. Zhao, and J. Prince, "Multi-atlas-based CT synthesis from conventional MRI with patch-based refinement for MRI-based radiotherapy planning," in *SPIE Med. Imag.*, vol. 10133, 2017, p. 101331I.
- [11] Y. Huang, L. Shao, and A. F. Frangi, "Simultaneous super-resolution and cross-modality synthesis of 3D medical images using weakly-supervised joint convolutional sparse coding," *Comput. Vis. Pattern Recognit.*, pp. 5787–5796, 2017.
- [12] —, "Cross-modality image synthesis via weakly coupled and geometry co-regularized joint dictionary learning," *IEEE Trans. Med. Imag.*, vol. 37, no. 3, pp. 815–827, 2018.
- [13] A. Adam, A. Dixon, J. Gillard, C. Schaefer-Prokop, R. Grainger, and D. Allison, *Grainger & Allison's Diagnostic Radiology*. Elsevier, 2014.
- [14] D. Ellison, S. Love, L. Chimelli, B. Harding, J. Lowe, H. Vinters, S. Brandner, and W. Yong, *Neuropathology: A Reference Text of CNS Pathology*. Elsevier, 2012.
- [15] C. Zhao, A. Carass, J. Lee, Y. He, and J. L. Prince, "Whole brain segmentation and labeling from CT using synthetic MR images," in *Mach. Learn. Med. Imag.*, 2017, pp. 291–298.
- [16] A. Jog, A. Carass, S. Roy, D. L. Pham, and J. L. Prince, "Random forest regression for magnetic resonance image synthesis," *Med. Image Anal.*, vol. 35, pp. 475–488, 2017.
- [17] H. Van Nguyen, K. Zhou, and R. Vemulapalli, "Cross-domain synthesis of medical images using efficient location-sensitive deep network," in *Med. Image Comput. Comput. Assist. Interv.*, 2015, pp. 677–684.
- [18] R. Vemulapalli, H. Van Nguyen, and S. K. Zhou, "Unsupervised cross-modal synthesis of subject-specific scans," in *Int. Conf. Comput. Vis.*, 2015, pp. 630–638.
- [19] Y. Wu, W. Yang, L. Lu, Z. Lu, L. Zhong, M. Huang, Y. Feng, Q. Feng, and W. Chen, "Prediction of CT substitutes from MR images based on local diffeomorphic mapping for brain PET attenuation correction," *J. Nucl. Med.*, vol. 57, no. 10, pp. 1635–1641, 2016.
- [20] D. C. Alexander, D. Zikic, J. Zhang, H. Zhang, and A. Criminisi, "Image quality transfer via random forest regression: Applications in diffusion MRI," in *Med. Image Comput. Comput. Assist. Interv.*, 2014, pp. 225–232.
- [21] T. Huynh, Y. Gao, J. Kang, L. Wang, P. Zhang, J. Lian, and D. Shen, "Estimating CT image from MRI data using structured random forest and auto-context model," *IEEE Trans. Med. Imag.*, vol. 35, no. 1, pp. 174–183, 2016.
- [22] P. Coupe, J. V. Manjón, M. Chamberland, M. Descoteaux, and B. Hiba, "Collaborative patch-based super-resolution for diffusion-weighted images," *NeuroImage*, vol. 83, pp. 245–261, 2013.
- [23] V. Seveltidis, M. V. Giuffrida, and S. A. Tsaftaris, "Whole image synthesis using a deep encoder-decoder network," in *Simul. Synth. Med. Imaging*, 2016, pp. 127–137.
- [24] A. Chartsias, T. Joyce, M. V. Giuffrida, and S. A. Tsaftaris, "Multimodal MR synthesis via modality-invariant latent representation," *IEEE Trans. Med. Imag.*, vol. 37, no. 3, pp. 803–814, 2018.
- [25] C. Bowles, C. Qin, C. Ledig, R. Guerrero, R. Gunn, A. Hammers, E. Sakka, D. Dickie, M. Hernández, N. Royle *et al.*, "Pseudo-healthy image synthesis for white matter lesion segmentation," in *Simul. Synth. Med. Imaging*, 2016, pp. 87–96.
- [26] N. Cordier, H. Delingette, M. Le, and N. Ayache, "Extended modality propagation: Image synthesis of pathological cases," *IEEE Trans. Med. Imag.*, vol. 35, pp. 2598–2608, 2016.
- [27] T. Joyce, A. Chartsias, and S. A. Tsaftaris, "Robust multi-modal MR image synthesis," in *Med. Image Comput. Comput. Assist. Interv.*, 2017, pp. 347–355.
- [28] W. Wei, E. Poirion, B. Bodini, S. Durrleman, O. Colliot, B. Stankoff, and N. Ayache, "Fluid-attenuated inversion recovery MRI synthesis from multisequence MRI using three-dimensional fully convolutional networks for multiple sclerosis," *J. Med. Imaging*, vol. 6, no. 1, p. 014005, 2019.
- [29] A. Beers, J. Brown, K. Chang, J. Campbell, S. Ostmo, M. Chiang, and J. Kalpathy-Cramer, "High-resolution medical image synthesis using progressively grown generative adversarial networks," *arXiv:1805.03144*, 2018.
- [30] S. U. Dar, M. Yurt, L. Karacan, A. Erdem, E. Erdem, and T. Çukur, "Image synthesis in multi-contrast MRI with conditional generative adversarial networks," *IEEE Trans. Med. Imag.*, vol. 38, no. 10, pp. 2375–2388, 2019.
- [31] B. Yu, L. Zhou, L. Wang, J. Fripp, and P. Bourgeat, "3D cGAN based cross-modality MR image synthesis for brain tumor segmentation," *Int. Symp. Biomed. Imaging*, pp. 626–630, 2018.
- [32] D. Nie, R. Trullo, J. Lian, L. Wang, C. Petitjean, S. Ruan, and Q. Wang, "Medical image synthesis with deep convolutional adversarial networks," *IEEE Trans. Biomed. Eng.*, vol. 65, no. 12, pp. 2720–2730, 2018.
- [33] K. Armanious, C. Jiang, M. Fischer, T. Küstner, T. Hepp, K. Nikolaou, S. Gatidis, and B. Yang, "MedGAN: Medical image translation using GANs," *Comput. Med. Imaging Grap.*, vol. 79, p. 101684, 2019.
- [34] D. Lee, J. Kim, W.-J. Moon, and J. C. Ye, "CollaGAN: Collaborative GAN for missing image data imputation," in *Comput. Vis. Pattern Recognit.*, 2019, pp. 2487–2496.
- [35] H. Li, J. C. Paetzold, A. Sekuboyina, F. Kofler, J. Zhang, J. S. Kirschke, B. Wiestler, and B. Menze, "DiamondGAN: Unified multi-modal generative adversarial networks for MRI sequences synthesis," in *Med. Image Comput. Comput. Assist. Interv.*, 2019, pp. 795–803.
- [36] T. Zhou, H. Fu, G. Chen, J. Shen, and L. Shao, "Hi-Net: Hybrid-fusion network for multi-modal MR image synthesis," *IEEE Trans. Med. Imag.*, vol. 39, no. 9, pp. 2772–2781, 2020.
- [37] H. Lan, A. Toga, and F. Sepehrband, "SC-GAN: 3D self-attention conditional GAN with spectral normalization for multi-modal neuroimaging synthesis," *bioRxiv:2020.06.09.143297*, 2020.
- [38] M. Yurt, S. U. Dar, A. Erdem, E. Erdem, K. K. Oguz, and T. Çukur, "mustGAN: multi-stream generative adversarial networks for MR image synthesis," *Med. Image Anal.*, vol. 70, p. 101944, 2021.
- [39] H. Yang, X. Lu, S.-H. Wang, Z. Lu, J. Yao, Y. Jiang, and P. Qian, "Synthesizing multi-contrast MR images via novel 3D conditional variational auto-encoding GAN," *Mob. Netw. Appl.*, vol. 26, pp. 1–10, 2021.
- [40] X. Wang, R. Girshick, A. Gupta, and K. He, "Non-local neural networks," in *Comput. Vis. Pattern Recognit.*, 2018, pp. 7794–7803.
- [41] N. Kodali, J. Hays, J. Abernethy, and Z. Kira, "On convergence and stability of GANs," *arXiv:1705.07215*, 2017.
- [42] O. Oktay, J. Schlemper, L. L. Folgoc, M. J. Lee, M. Heinrich, K. Misawa, K. Mori, S. G. McDonagh, N. Hammerla, B. Kainz *et al.*, "Attention U-Net: Learning where to look for the pancreas," *arXiv:1804.03999*, 2018.
- [43] H. Zhang, I. Goodfellow, D. Metaxas, and A. Odena, "Self-attention generative adversarial networks," in *Int. Conf. Mach. Learn.*, vol. 97, 2019, pp. 7354–7363.
- [44] S. A. Kamran, K. F. Hossain, A. Tavakkoli, S. L. Zuckerbrod, K. M. Sanders, and S. A. Baker, "VTGAN: Semi-supervised retinal image synthesis and disease prediction using vision transformers," *arXiv:2104.06757*, 2021.
- [45] H.-C. Shin, A. Ihsani, S. Mandava, S. T. Sreenivas, C. Forster, J. Cha, and A. D. N. Initiative, "GANBERT: Generative adversarial networks with bidirectional encoder representations from transformers for MRI to PET synthesis," *arXiv:2008.04393*, 2020.
- [46] X. Zhang, X. He, J. Guo, N. Ettehadi, N. Aw, D. Semanek, J. Posner, A. Laine, and Y. Wang, "PTNet: A high-resolution infant MRI synthesizer based on transformer," *arXiv:2105.13993*, 2021.
- [47] O. Dalmaz, M. Yurt, and T. Çukur, "ResViT: Residual vision transformers for multi-modal medical image synthesis," *IEEE Trans Med Imaging*, vol. 44, no. 10, pp. 2598–2614, 2022.
- [48] A. Dosovitskiy, L. Beyer, A. Kolesnikov, D. Weissenborn, X. Zhai, T. Unterthiner, M. Dehghani, M. Minderer, G. Heigold, S. Gelly *et al.*, "An image is worth 16x16 words: Transformers for image recognition at scale," *arXiv:2010.11929*, 2021.
- [49] H. A. Bedel, I. Sivgin, O. Dalmaz, S. U. Dar, and T. Çukur, "Bolt: Fused window transformers for fmri time series analysis," *Med Image Anal*, vol. 88, p. 102841, 2023.
- [50] Z. Zhang, L. Yu, X. Liang, W. Zhao, and L. Xing, "TransCT: Dual-path transformer for low dose computed tomography," in *Med. Image Comput. Comput. Assist. Interv.*, 2021, pp. 55–64.
- [51] L. Zhu, B. Liao, Q. Zhang, X. Wang, W. Liu, and X. Wang, "Vision mamba: Efficient visual representation learning with bidirectional state space model," *arXiv:2401.09417*, 2024.
- [52] Y. Liu, Y. Tian, Y. Zhao, H. Yu, L. Xie, Y. Wang, Q. Ye, and Y. Liu, "Vmamba: Visual state space model," *arXiv:2401.10166*, 2024.
- [53] R. Xu, S. Yang, Y. Wang, Y. Cai, B. Du, and H. Chen, "Visual mamba: A survey and new outlooks," 2024. [Online]. Available: <https://arxiv.org/abs/2404.18861>
- [54] X. Liu, C. Zhang, and L. Zhang, "Vision mamba: A comprehensive survey and taxonomy," 2024. [Online]. Available: <https://arxiv.org/abs/2405.04404>
- [55] J. Ma, F. Li, and B. Wang, "U-mamba: Enhancing long-range dependency for biomedical image segmentation," *arXiv:2401.04722*, 2024.
- [56] Z. Xing, T. Ye, Y. Yang, G. Liu, and L. Zhu, "Segmamba: Long-range sequential modeling mamba for 3d medical image segmentation," *arXiv:2401.13560*, 2024.
- [57] J. Ruan and S. Xiang, "VM-UNet: Vision Mamba UNet for Medical Image Segmentation," *arXiv:2402.02491*, 2024.
- [58] Y. Yue and Z. Li, "Medmamba: Vision mamba for medical image classification," *arXiv:2403.03849*, 2024.
- [59] V. Kearney, B. P. Ziemer, A. Perry, T. Wang, J. W. Chan, L. Ma, O. Morin, S. S. Yom, and T. D. Solberg, "Attention-aware discrimination for MR-to-CT image translation using cycle-consistent generative adversarial networks," *Radiol. Artif. Intell.*, vol. 2, no. 2, p. e190027, 2020.
- [60] J. Zhao, D. Li, Z. Kassam, J. Howey, J. Chong, B. Chen, and S. Li, "Tripartite-GAN: Synthesizing liver contrast-enhanced MRI to improve tumor detection," *Med. Image Anal.*, vol. 63, p. 101667, 2020.



- [61] Z. Yuan, M. Jiang, Y. Wang, B. Wei, Y. Li, P. Wang, W. Menpes-Smith, Z. Niu, and G. Yang, "SARA-GAN: Self-attention and relative average discriminator based generative adversarial networks for fast compressed sensing MRI reconstruction," *Front. Neuroinform.*, vol. 14, p. 58, 2020.
- [62] M. Li, W. Hsu, X. Xie, J. Cong, and W. Gao, "SACNN: Self-attention convolutional neural network for low-dose CT denoising with self-supervised perceptual loss network," *IEEE Trans. Med. Imag.*, vol. 39, no. 7, pp. 2289–2301, 2020.
- [63] Y. Xie, J. Zhang, C. Shen, and Y. Xia, "CoTr: Efficiently bridging CNN and transformer for 3D medical image segmentation," *arXiv:2103.03024*, 2021.
- [64] J. Chen, Y. Lu, Q. Yu, X. Luo, E. Adeli, Y. Wang, L. Lu, A. L. Yuille, and Y. Zhou, "TransUNet: Transformers make strong encoders for medical image segmentation," *arXiv:2102.04306*, 2021.
- [65] Y. Dai and Y. Gao, "TransMed: Transformers advance multi-modal medical image classification," *arXiv:2103.05940*, 2021.
- [66] Y. Luo, Y. Wang, C. Zu, B. Zhan, X. Wu, J. Zhou, D. Shen, and L. Zhou, "3D Transformer-GAN for high-quality PET reconstruction," in *Med. Image Comput. Comput. Assist. Interv.*, 2021, pp. 276–285.
- [67] Y. Korkmaz, S. U. H. Dar, M. Yurt, M. Ozbey, and T. Cukur, "Unsupervised MRI reconstruction via zero-shot learned adversarial transformers," *IEEE Trans Med Imaging*, vol. 41, no. 7, pp. 1747–1763, 2022.
- [68] P. Isola, J.-Y. Zhu, T. Zhou, and A. A. Efros, "Image-to-image translation with conditional adversarial networks," *Comput. Vis. Pattern Recognit.*, pp. 1125–1134, 2017.
- [69] K. He, X. Zhang, S. Ren, and J. Sun, "Deep residual learning for image recognition," in *Comput. Vis. Pattern Recognit.*, 2016, pp. 770–778.
- [70] I. Tolstikhin, N. Houlsby, A. Kolesnikov, L. Beyer, X. Zhai, T. Unterthiner, J. Yung, A. Steiner, D. Keysers, J. Uszkoreit *et al.*, "Mlp-mixer: An all-mlp architecture for vision," 2021.
- [71] L.-H. Chen, C. G. Bampis, Z. Li, C. Chen, and A. C. Bovik, "Convolutional block design for learned fractional downsampling," *arXiv:2105.09999*, 2021.
- [72] T. Nyholm, S. Svensson, S. Andersson, J. Jonsson, M. Sohlén, C. Gustafsson, E. Kjellén, K. Söderström, P. Albertsson, L. Blomqvist *et al.*, "MR and CT data with multiobserver delineations of organs in the pelvic area—part of the gold atlas project," *Med. Phys.*, vol. 45, no. 3, pp. 1295–1300, 2018.
- [73] M. Jenkinson and S. Smith, "A global optimisation method for robust affine registration of brain images," *Med. Image Anal.*, vol. 5, pp. 143–156, 2001.
- [74] D. P. Kingma and J. Ba, "Adam: A method for stochastic optimization," in *Int. Conf. Learn. Represent.*, 2015.
- [75] A. Sharma and G. Hamarneh, "Missing MRI pulse sequence synthesis using multi-modal generative adversarial network," *IEEE Trans. Med. Imag.*, vol. 39, pp. 1170–1183, 2020.
- [76] G. Elmas, S. U. Dar, Y. Korkmaz, E. Ceyani, B. Susam, M. Özbey, S. Avestimehr, and T. Çukur, "Federated Learning of Generative Image Priors for MRI Reconstruction," *IEEE Trans Med Imaging*, vol. 42, no. 7, pp. 1996–2009, 2023.
- [77] O. Dalmaz, M. U. Mirza, G. Elmas, M. Ozbey, S. U. Dar, E. Ceyani, K. K. Oguz, S. Avestimehr, and T. Çukur, "One model to unite them all: Personalized federated learning of multi-contrast MRI synthesis," *Med Image Anal*, vol. 94, p. 103121, 2024.
- [78] J. Wolterink, A. M. Dinkla, M. Savenije, P. Seevinck, C. Berg, and I. Išgum, "Deep MR to CT synthesis using unpaired data," in *Simul. Synth. Med. Imaging*, 2017, pp. 14–23.
- [79] C.-B. Jin, H. Kim, M. Liu, W. Jung, S. Joo, E. Park, Y. S. Ahn, I. H. Han, J. I. Lee, and X. Cui, "Deep CT to MR synthesis using paired and unpaired data," *Sensors*, vol. 19, no. 10, p. 2361, 2019.
- [80] Y. Ge, D. Wei, Z. Xue, Q. Wang, X. Zhou, Y. Zhan, and S. Liao, "Unpaired MR to CT synthesis with explicit structural constrained adversarial learning," in *Int. Symp. Biomed. Imaging*, 2019, pp. 1096–1099.
- [81] B. Zhan, D. Li, Y. Wang, Z. Ma, X. Wu, J. Zhou, and L. Zhou, "LR-cGAN: Latent representation based conditional generative adversarial network for multi-modality MRI synthesis," *Biomed. Signal Process. Control*, vol. 66, p. 102457, 2021.
- [82] D. Nie and D. Shen, "Adversarial Confidence Learning for Medical Image Segmentation and Synthesis," *Int. J. Comput. Vision*, vol. 128, no. 10, pp. 2494–2513, 2020.
- [83] M. Özbey, S. U. Dar, H. A. Bedel, O. Dalmaz, Ş. Öztürk, A. Güngör, and T. Çukur, "Unsupervised medical image translation with adversarial diffusion models," *IEEE Trans Med Imaging*, vol. 42, no. 12, pp. 3524–3539, 2023.
- [84] P. Dhariwal and A. Nichol, "Diffusion models beat gans on image synthesis," in *Adv Neural Inf Process Syst*, vol. 34, 2021, pp. 8780–8794.
- [85] F. Arslan, B. Kabas, O. Dalmaz, M. Ozbey, and T. Çukur, "Self-consistent recursive diffusion bridge for medical image translation," *arXiv:2405.06789*, 2024.
- [86] Z. Wang, Y. Yang, Y. Chen, T. Yuan, M. Sermesant, H. Delingette, and O. Wu, "Mutual information guided diffusion for zero-shot cross-modality medical image translation," *IEEE Trans Med Imaging*, pp. 1–1, 2024.
- [87] A. Güngör, S. U. Dar, Ş. Öztürk, Y. Korkmaz, G. Elmas, M. Özbey, and T. Çukur, "Adaptive diffusion priors for accelerated MRI reconstruction," *Med Image Anal*, vol. 88, p. 102872, 2023.
- [88] M. U. Mirza, O. Dalmaz, H. A. Bedel, G. Elmas, Y. Korkmaz, A. Gungor, S. U. Dar, and T. Çukur, "Learning Fourier-Constrained Diffusion Bridges for MRI Reconstruction," *arXiv:2308.01096*, 2023.
- [89] J. Kim and J. C. Ye, "HiCBridge: Resolution enhancement of hi-c data using direct diffusion bridge," 2024. [Online]. Available: <https://openreview.net/forum?id=RUVzlotXY0>
- [90] Y. Korkmaz, T. Cukur, and V. M. Patel, "Self-supervised mri reconstruction with unrolled diffusion models," in *MICCAI*, 2023, pp. 491–501.
- [91] H. A. Bedel and T. Çukur, "DreaMR: Diffusion-driven counterfactual explanation for functional MRI," *arXiv:2307.09547*, 2023.
- [92] J. Liu, H. Yang, H.-Y. Zhou, Y. Xi, L. Yu, Y. Yu, Y. Liang, G. Shi, S. Zhang, H. Zheng *et al.*, "Swin-umamba: Mamba-based unet with imagenet-based pretraining," *arXiv:2402.03302*, 2024.